STRATEGIC ASTROPHYSICS TECHNOLOGY

DEVELOPMENT

Technology Milestone White Paper

Dual-Purpose Focal Plane Mask

J. Kent Wallace, PI
Garreth Ruane
Nasrat A. Raouff
A. J. Eldorado Riggs
Camilo Mejia Prada
Tobias Wenger

Jet Propulsion Laboratory, California Institute of Technology

15 February 2023
Revision 1st: 15 May 2023
Revision 2nd: 11 Sept 2023
Revision 3rd: 9 Nov 2023

National Aeronautics and Space Administration
Jet Propulsion Laboratory
California Institute of Technology
Pasadena, California

Approvals:

Released by

E-SIGNED by James Wallace
on 2023-11-16 00:20:11 GMT

_____ _____
J. Kent Wallace **Date**
Principal Investigator

Approved by

E-SIGNED by Brendan Crill
on 2023-11-13 23:59:41 GMT

_____ _____
Brendan Crill **Date**
Exoplanet Exploration Deputy Program Chief Technologist, JPL

E-SIGNED by Nicholas Siegler
on 2023-11-14 02:03:56 GMT

_____ _____
Nick Siegler **Date**
Exoplanet Exploration Program Chief Technologist, JPL

E-SIGNED by Doug Hudgins
on 2023-11-17 01:10:39 GMT

_____ _____
Douglas Hudgins **Date**
Exoplanet Exploration Program Scientist, NASA HQ

Table of Contents

1. Objective

The objective of this activity is to demonstrate the active wavefront sensing and control using out-of-band light to contemporaneously maintain high-contrast imaging in the science focal plane. This closed-loop wavefront sensing and control will allow for a significant reduction in the system level observatory requirements either using natural guide stars or optical beacons independent of the science target for more rapid and accurate sensing and control.

1.1 Goals

We will perform a laboratory demonstration of a dual-purpose focal plane mask (combining wavefront sensing and high-contrast capabilities) that will be used to sense and stabilize the wavefront required for imaging exoplanets. During the first year of the work we will specify, design and procure the custom focal plane mask. This will involve detailed coating design and analysis of the impact on both wavefront sensing and coronagraphic imaging. After the design and specification is complete, we will place a procurement subcontract for first generation devices.

The second year will involve the installation of the mask on the high-contrast imaging testbed. This device will be entirely compatible with the existing infrastructure and should not impose any other needs on the rest of the system. Once installed we will use the device in its two main modes: 1) wavefront sensing and 2) high-contrast imaging. We will initially test these capabilities independently before combining their functionality. The separate functionalities will be tested independently as follows: 1) when used for wavefront sensing, the dual-purpose focal plane mask will be used to measure a wavefront with sensing precision at the picometer level using a wavelength specific to wavefront sensing 2) when used for high contrast imaging, the device will be demonstrated to create starlight rejection that is consistent with the direct detection of exoplanets.

The third year will demonstrate using the wavefront sensing and high-contrast imaging modes simultaneously and with a closed-loop system that will enable maintaining the state of the system in the presence of fast vibrations as well as long-term drifts. This ultimate objective will demonstrate in the clearest possible way the feasibility of active stabilization of the optical wavefront and, as a result, the final image contrast.

This proposal will advance the technology readiness level (TRL) of this method from TRL3 to TRL4. To date, both analytical and laboratory studies have been done to demonstrate the viability. Here, the hardware and method are tested comprehensively as an ensemble.

1.2 Expected Significance

A successful demonstration of the active wavefront stabilization that is in support of and contemporaneous with high-contrast imaging has the potential to fundamentally change the requirements that high contrast imaging imposes on future flagship telescopes such as the Habitable Worlds Observatory. Currently, many in the exoplanet engineering community believe that the optical systems must be architected for long-term stability at the picometer level over all timescales. That is a very difficult engineering challenge. The technical approach presented here fundamentally changes the problem from building a picometer-stable telescope to building a system with looser opto-mechanical stability requirements that can be actively controlled to meet

the wavefront stability requirements. In so doing, the resulting actively controlled system may be more feasible from an engineering standpoint, potentially lower the cost of the mission, and will be much more robust to addressing unexpected and unanticipated instabilities in flight.

1.3 Perceived Impact to State of Knowledge

At the heart of this proposal is the idea of advancing the concept that all future space-based telescopes and instruments should be viewed as active rather than passive systems. Such a change in perspective is actually reflected in the technologies which enabled the first direct detection of exoplanets from the ground – adaptive optics. If it were not possible to remove the blurring effects of the earth's atmosphere from ground-based telescopes – sharply imaging exoplanets would be impossible. Here, we apply the same method of sensing and actively correcting time-varying optical errors to space telescopes and instrumentation. This active system enables some acceptable level of dynamics and disturbances in the system.

However, there are greater implications as well. The fundamental architecture whereby some light is reflected from a focal plane window for active sensing while science light is transmitted can have wide applicability to other science imaging applications. For instance, *any* cover window before a detector focal plane array can be replaced with a dual-purpose mask as proposed here and thus enable continual wavefront sensing for any science observation.

1.4 Relevance to Element Programs and Objectives in the NOFO

The SAT is specifically established to develop NASA technologies for future missions. The Astro2020 decadal report, recently released, specifically endorses a 6-meter observatory for direct detection and characterization of exoplanets – the Habitable Worlds Observatory. This proposal addresses the technical challenges of this flagship mission in such a way as to significantly relax telescope and system level requirements while also reducing costs and ensuring mission reliability. This is no small matter. The capability to directly image exoplanets in reflected, visible light imposes unprecedented wavefront stability requirements that may never be possible to demonstrate with the end-to-end system prior to launch. However, the proposed wavefront sensing and control can be fully characterized at the instrument level using a telescope simulator and potentially provide the confidence that the contrast requirements will be achieved in orbit.

2. The Dual-Purpose focal plane mask

The dual-purpose focal plane mask combines the capabilities of two technologies which have already been separately and independently demonstrated: 1) the focal-plane mask coronagraph and 2) the Zernike (or "phase-contrast") wavefront sensor. Combining the two into a single focal-plane device, and using non-overlapping spectral photons will enable contemporaneous operation of both the high-contrast science image and the wavefront sensor. The common element ensures the wavefront is measured where it matters – at the coronagraph mask.

2.1 Focal plane mask description

Visible-light coronagraphs use a pair of deformable mirrors and an occulting or diffractive focal plane mask to suppress starlight while allowing imaging of exoplanets orbiting the star. This technique will be demonstrated in flight for the first time by the Roman Space Telescope (RST) coronagraph instrument. RST will also demonstrate a low-order wavefront control loop using light reflecting from the occulting spot in its Lyot-style coronagraphs. While RST will raise the system-

level technology readiness of coronagraph instruments for future flagship missions, there are some very important differences in the wavefront error requirements and component level design as compared to a mission like the Habitable Worlds Observatory. Future flagships will require better wavefront stability using a larger, and potentially segmented, telescope.

To this end, we introduce a modification to the RST coronagraph instrument wavefront sensor design. Rather than using the light reflected by the occulting spot, which has a low pass filtering effect, we propose to use the light across a much larger region of the image plane to allow for higher order wavefront sensing. To demonstrate this, we manufactured a fully reflective focal plane mask and installed it on the Decadal Survey Testbed (DST) in HCIT (see Fig. 1; Ruane et al. 2020). The focal plane mask was specially designed to work as a Zernike wavefront sensor (Zernike 1932, Dicke 1975), which uses a small circular dimple at the focal plane to convert phase variations in the plane of the DM to intensity variations at the wavefront sensing camera. We were then able to introduce known patterns on one of the DMs and measure the resulting change in wavefront. Figure 2 shows the reconstructed changes in the wavefront for low order variations in the form of Zernike polynomials as well as mid spatial frequency variations in the form of Fourier modes. The latter would not be possible using the low-order wavefront sensor on RST's coronagraph instrument. The artifacts are due to either non-response actuators on the imaged DM or by similar non-responsive actuators in the 'out of plane' DM. They represent the realities of the DMs currently used in the system. However, the actuators that can be controlled, are controlled, and the non-responsive ones persist in their state. For our demonstration, the artifacts play no role in sensing and control. Using the same system, we also demonstrated picometer level sensitivity at high spatial resolution (see Fig. 3b). Indeed, the DM poke pattern in Fig. 3b is for a single bit of the DM electronics which corresponds to ~ 10 picometer surface height – the minimum incremental increase.

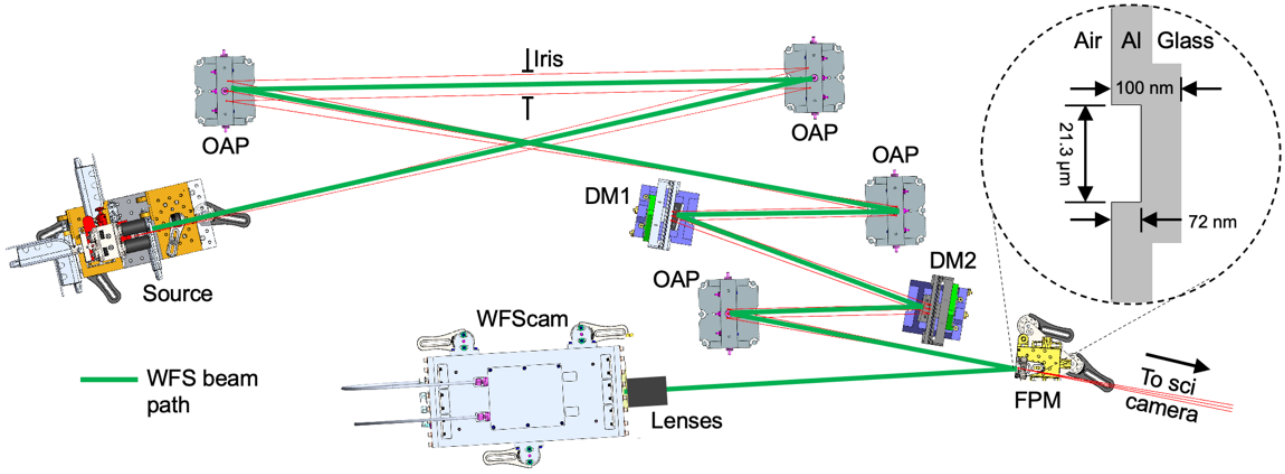

Figure 1. The fully-reflective Zernike wavefront sensor installed on the DST in HCIT. A small (21.3 um diameter) circular phase dimple (72 nm in depth) in an aluminum coated substrate was used to convert phase variations to intensity variations at the wavefront sensing camera.

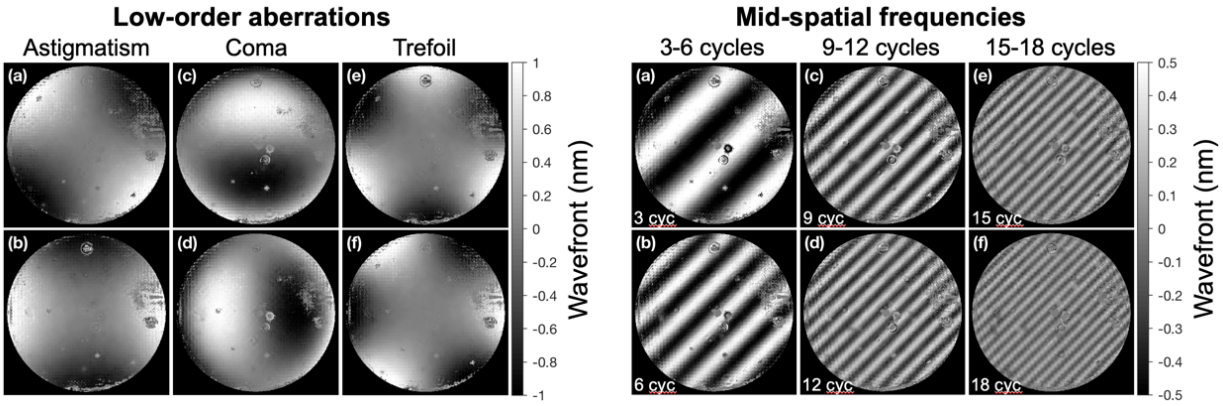

Figure 2. Example wavefront variations introduced on the DM and measured using the reflective Zernike wavefront sensor shown in Fig. 1.

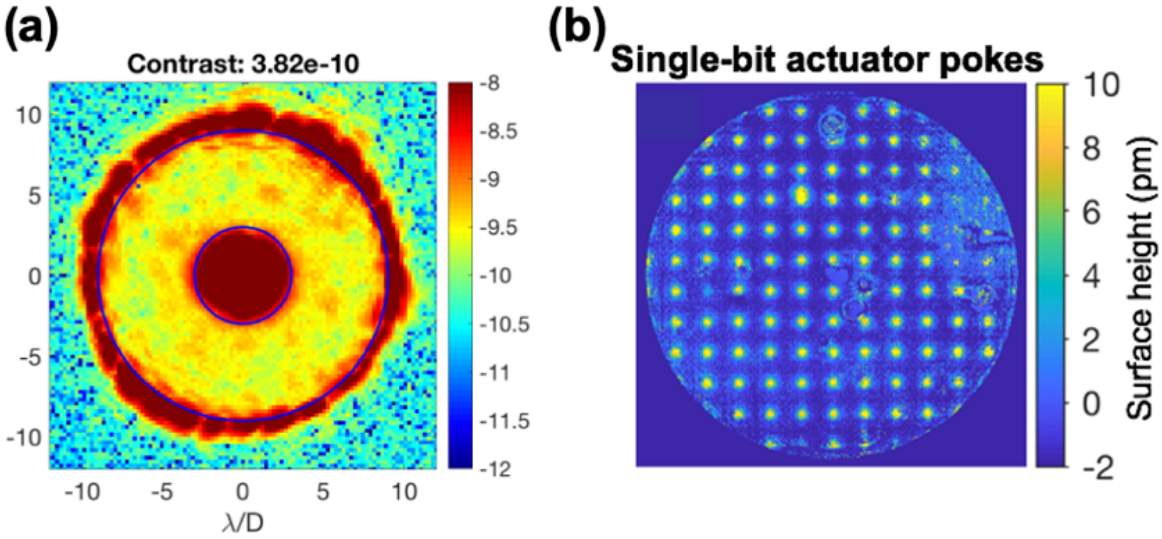

Figure 3. Past results from the Decadal Survey Testbed (DST) in NASA's High Contrast Imaging Testbed (HCIT) facility. (a) A dark hole showing a mean raw contast of <4e-10 in a 10% bandwidth over 3-8 λ/D (Seo et al., 2019). (b) A measurement in the change of a DM surface in the DST using a non-simultaneous, reflective Zernike wavefront sensor. The grid corresponds to a change in the lowest significant bit in the DM electronics which is also ~ 10 picometer surface height change. (Ruane et al, 2020).

The proposed technology is designed to make the same measurement as the reflective Zernike wavefront sensor makes in Fig. 3b, but contemporaneously with the high-contrast imaging on the coronagraph's science camera. This is achieved by modifying the focal plane mask design to include a dichroic coating on the focal plane mask substrate (see Fig. 4). For example, if the high-contrast imaging is occurring in a red band, the focal plane mask is designed to act as a conventional coronagraph mask and the substrate transmits red wavelengths. For a Lyot coronagraph, this may be achieved using a circle of Ni or other mostly-opaque metal a few λ/D across. The wavefront sensing would then occur in a blue band, which is reflected by both the Ni

and dichroic coating. A phase dimple (~λ/D in diameter) in the Ni coating would then act as the wavefront sensing mask. We have envisioned a number of variations on this design scheme that use combinations of Ni and dielectric masks (e.g. materials currently used for the RST hybrid Lyot coronagraph masks (Trauger 2011) as well as more exotic coronagraph types, like vortex coronagraphs (Mawet 2009).

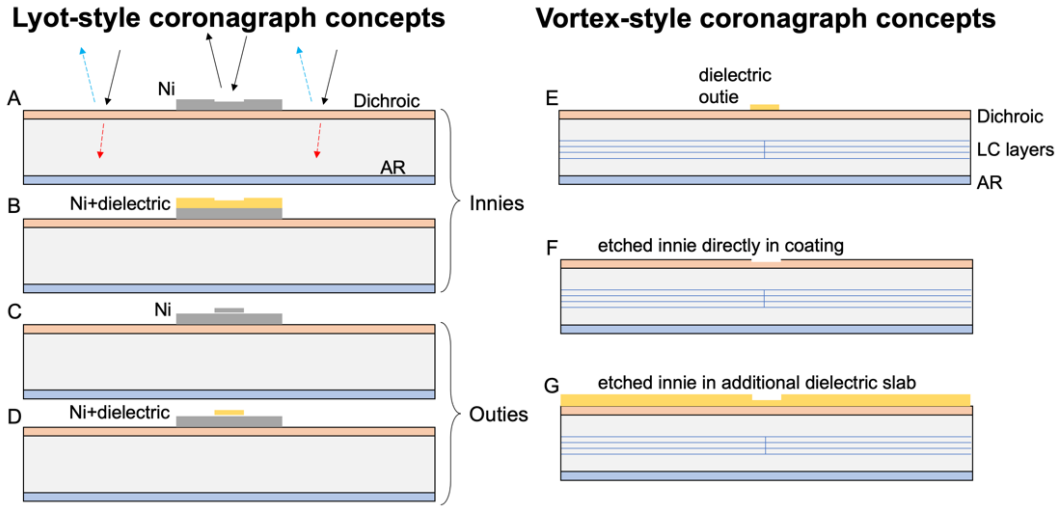

Figure 4. Examples of dual-purpose masks for simultaneous high contrast imaging and high order wavefront sensing.

The phase dimples used here for wavefront are motivated by the fact that a Zernike wavefront sensor has nearly optimal sensitivity to phase changes (Guyon 2005; Ruane 2020). Integrating the coronagraph and wavefront sensing masks is optimal because the wavefront is sensed after the DMs to allow for closed-loop wavefront control. Furthermore, there is no need to introduce a beamsplitter upstream of the focal plane mask for wavefront sensing as proposed in the LUVOIR report. Such as beam splitter would introduce ghost beams due to imperfect AR coatings, which would make it impossible to achieve high contrast in the coronagraph over broad bandwidths. Thus, the dual-purpose mask is currently the only viable solution for making direct higher-order wavefront measurements at the position just before the focal plane mask, where it matters the most.

3. Milestone Definition

Designing a focal plane mask that performs both wavefront sensing for mid-spatial frequencies while simultaneously serving as the coronagraphic mask is challenging. However, there is some heritage to leverage namely, from the Coronagraph Instrument (CGI) on the Roman Space Telescope. In that particular case, placing a Zernike phase dimple of diameter ~ 1 diffraction diameter wide on top of a ~ 5 diffraction diameter wide absorbing occulting mask was straightforward because: 1) only low-order modes were sensed and 2) because the dimple is on the occulting mask, there was little impact to the coronagraph. To sense higher-order spatial frequency modes in the CGI architecture requires that the nickel occulting mask grow in diameter, which is simply not feasible.

Our approach is therefore to use two different spectral bands to separate out the functions of wavefront sensing and high-contrast imaging. Thus, we envision a focal plane mask with the

following features: a) a central ~ 1 lambda/D portion that has a Zernike-like phase dimple in reflection in one band, and b) the same central portion appearing to occult the central ~ few lambda/D portion in transmission for the science band. This will require some careful coating and manufacturing design analysis, and although we currently have no specific design, we have multiple paths to pursue.

Our method of technical/scientific development will proceed as follows:

- Design dichroic optical filters to efficiently separate the two spectral bands.
- Perform detailed numerical analysis of these focal plane masks to access the performance for both wavefront sensing and coronagraphy.
- Develop the requirements and specifications for these custom focal plane masks.
- Place a procurement subcontract in order to manufacture these devices from commercial optics/coatings vendors.
- Install, align, operate and characterize the first focal plane device.
    - Establish preliminary operation in three different modes:
        1. Wavefront sensing
        2. High-contrast imaging
        3. Closed-loop wavefront control.
- Reiterate the design and analysis for the second-generation dual-purpose focal plane masks.
- Install, align and characterize the second-generation device
- Perform full operation of the new device.

The greatest challenge of this development is also the riskiest – development of the focal plane mask. The heritage of the method, as mentioned previously, was narrowly focused on low-order sensing. The extension to dual spectral bands and sensing higher spatial frequencies is non-trivial. Our engineering expertise in coatings will guide this development. Other aspects of the development, including the operation of the HCIT are not seen as particularly challenging given that our team members have extensive knowledge of the operation. Indeed, the facility is so well developed that our use of it does not impose a significant challenge.

<u>During the mask testing in HCIT, we aim to achieve the following milestones:</u>

Milestone 1: Demonstrate a mean raw contrast of 1e-9 within a dark hole region 3-10 λ/D from the star on a coronagraph testbed using any visible wavelength and bandwidth.

Our preference is to achieve this in a 10% bandwidth with a two-sided dark hole. However, we consider a one-sided dark hole in monochromatic light as our success threshold. In this way, issues with broadband starlight suppression will not prevent us from moving on to our subsequent milestones as these are often due to testbed sources of incoherent or chromatic residuals and won't necessarily impact our lessons learned for simultaneous wavefront sensing and control. In our experience, HCIT testbeds can readily achieve 1e-9 in monochromatic light without the need for time consuming debugging exercises.

Milestone 2: Demonstrate <10 pm wavefront sensing sensitivity for low-order and mid-spatial frequency modes using light outside of a 20% bandwidth reserved for science.

Wavefront errors shall be injected with 10 pm RMS using a calibrated DM. The spatial modes shall include Noll-ordered Zernike polynomials Z4-Z11 (e.g. Fig. 2, left panel); Fourier modes with 5, 10, and 15 cycles across the pupil (e.g. Fig. 2, right panel); and single isolated actuator pokes (e.g. Fig. 3b). Each will be shown to have a repeatability of 1 pm RMS after averaging many repeated measurements following the procedure of Steeves et al (2020). The single isolated actuator poke will be used to demonstrate a noise floor of 1 pm RMS in flat region of the DM away from poked actuator(s) as in Ruane et al. (2020).

Here, sensitivity of the Zernike sensor relates the uncertainty of the phase difference measurement to the uncertainty of the measured intensity differences. The sensitivity relates the ability to estimate the phase in the presence of noise. In previous papers (Steeves and Ruane) we have explored the sensitivity mathematically and numerically. The expression for sensitivity in both papers are identical, with slightly different notations. Here we follow the notation of Steeves in the supplement. First, the phase signal is estimated from two intensity measurements: I_Z and I_P. The pupil intensity measured when the PSF is centered on the Zernike dimple is I_Z. The pupil intensity when off the dimple is I_P. A third intensity most be modeled. That intensity is due to the light that is low spatial frequency filtered by the action of the dimple in the focal plane mask. This modeled intensity is known as I_b. For the case when the phase change at the dimple is equal to $\pi/2$, the expression for the phase is given by:

$$\varphi(\boldsymbol{x}) - \beta(\boldsymbol{x}) = \frac{\pi}{4} + \arcsin\left[\frac{I_z - I_P - 2I_b}{2\sqrt{I_p 2\, I_b}}\right]$$

Here, β is the phase of the low-spatial-frequency filtered light passing through the focal plane mask dimple. Again, both I_b and β are numerically modeled. For small phase changes when the wavefront is nearly perfect, this expression becomes:

$$\Delta\varphi = \frac{\Delta Iz}{2\sqrt{I_p I_b}}, (radians)$$

The error on this phase difference is given by the standard deviation:

$$\sigma_{\Delta\varphi} = \frac{\sigma_{\Delta Iz}}{2\sqrt{I_P I_b}} = \frac{1}{\sqrt{N}} \frac{\sqrt{\Phi\, \tau\, QE + I_d\, \tau + N_r}}{\sqrt{2\, I_p I_b}}$$

In this expression, Φ is the source flux (in photons per second), τ is the integration time, QE is the detector quantum efficiency, I_d is the dark current and N_r is the read noise. This expression is the error after a series of N measurements based upon random noise sources alone.

For phase reconstruction, there are two methods to consider: 1) the interaction matrix approach and 2) the analytic approach. For this work, we will be using the interaction matrix approach because its more appropriate for measuring phase changes in the small phase error regime. This method is similar to the approach used by typical adaptive optics systems. The forward process of measuring the change in response of the sensor to a change in an actuator or a mode of the deformable mirror result in a response matrix. This is then inverted to create the interaction matrix, whereby measured changes in intensity are used to estimate the change in the deformable mirror. This is the baseline method that will be used to control the DM for these milestones.

The analytical reconstruction algorithm uses intensity measurements of *Ip* and *Iz*, then we model I_b (the low-spatially-filtered intensity. The arcsin expression is used to estimate the phase in the input pupil, ϕ. This method is well better suited for measuring absolute phase, but is model dependent. We note too that the repeatability of the DM commanded positions appears to be well below the picometer levels that we will be sensing and controlling. There is no reason to suggest that the DM or the DM electronics will in any way limit our performance goals.

Milestone 3: Demonstrate closed-loop control of at least one low-order and one mid-spatial-frequency disturbance with an OPD variance rejection factor of 10.
With the DMs set to achieve the best possible dark hole (success criteria: raw contrast of <1e-8 in 3-10 lambda/D dark hole at any wavelength or bandwidth), spatial modes including Zernike polynomials (Noll-ordered Z4-Z11) and Fourier modes (5, 10, and 15 cycles across the pupil) will be injected at a 0.01 Hz frequency using a calibrated DM. Wavefront sensor measurements will be used to apply a correction to the DM voltages in order to compensate for the injected disturbance. The wavefront sensor shall use any wavelength or bandwidth outside of the 20% bandwidth reserved for science. Our success criteria are to demonstrate an OPD variance rejection factor of 10 for a 100 pm RMS disturbance (yielding 30 pm RMS residuals). During the experiment, the effective noise in the wavefront sensor images will be adjusted to replicate a 6-meter telescope that uses the light of a m_V=2 natural guide star to correct a 30 pm RMS disturbance oscillating at 1 Hz down to 10 pm RMS (10× improvement in OPD variance) with an AO system running at 100 Hz.

The justification of the flight-equivalent scenario in milestone 3 is motivated by what is feasible for a 6-meter IR/O/UV flagship mission. We simulated a relevant scenario following the analytical modeling approach from Potier et al. (2021) and reference therein. Table 1-1 below provides the simulated parameters, which predicts 7.5 pm RMS wavefront error residuals with a m_V=2 star and control loop rate of 100 Hz.

Table 1-1. These parameters were used for the performance simulations for active rejection.

Parameter	Value
Telescope diameter	6.0 m
WFS band	V (λ_{center}= 550 nm)
WFS spectral bandwidth	100 nm
Guide star magnitude	2.0
Total flux incident on primary mirror	4.5e10 photons/sec
Transmission to WFS camera	0.3
WFS exposure time	0.01 sec
Residual closed-loop wavefront error	8.6e-5 rad RMS or 7.5 pm RMS

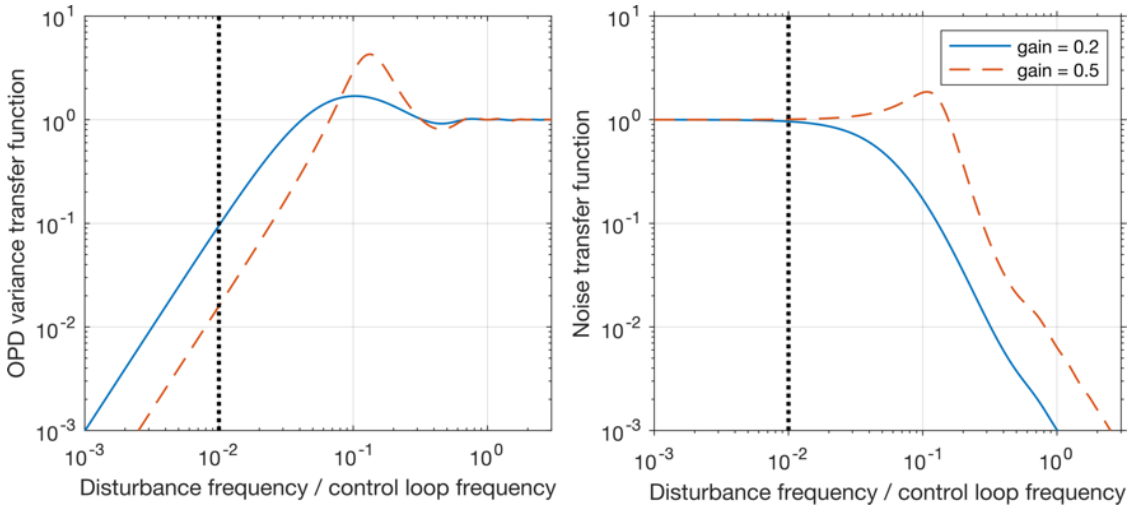

Figure 5. Control loop transfer function models using analytical method in Potier et al. (2021). Left panel: Transfer function that multiplies the initial power spectral density (PSD), assuming a lag time of 1 control loop period. With control loop frequency that is 100 times faster than the disturbance frequency, we expect a rejection factor of 10 for a proportional gain of ≥20%. Right panel: The noise transfer function (NTF) multiplies the noise PSD, which is then added to the final PSD. In the regime where the control loop is >100 times faster than the disturbance, the NTF is ~1. Using a gain that is too large can amplify high temporal frequency wavefront errors.

Control performance justification: Figure 5 (left panel) shows the OPD variance transfer function for an integrating controller, which multiplies the input power spectral density (PSD) of a given mode to estimate the resulting closed loop OPD variance. In the regime where the disturbance frequency is much smaller than the control loop frequency, the OPD variance is suppressed by a factor that has a power law dependence versus frequency. For a disturbance frequency that is 100 times faster than the control loop frequency, we expect a rejection factor of 10 using a proportional gain of 20% for the control loop and a lag time that is equal to the loop period. Meanwhile, noise in the wavefront sensor images adds to the closed-loop OPD variance with a noise transfer function close to unity and does not amplify the noise at higher frequencies as would be the case for a larger proportional gain (see Fig. 5, right panel). Therefore, in this scenario, the expected closed-loop OPD variance will simply be 0.1×(initial variance) + noise. During our experiment, we first compare the performance for an initial proportional gain setting of 20%, and then seek to find the optimal gain empirically, with the goal of further suppressing the initial variance such that the total closed-loop variance is ≥10× smaller than that of the injected disturbance. These transfer functions are strawman models and have not been measured in the lab.

Realistic noise levels: The noise in the wavefront sensor images in HCIT will be a combination of detector noise and photon noise. However, we assume that a flight-mission would employ photon-counting detectors. Our experimental approach will be to match the total noise in our images to the flight-equivalent scenario described above. We expect 5.3e9 photons/sec to be available from wavefront sensing in flight for an m_V=2 star. Assuming 32 pixels across the beam at the WFS camera, for example, this corresponds to a noise level of ~250 electrons per pixel in a 0.01 sec exposure. We will ensure that the HCIT WFS images include realistic noise by estimating and scaling the noise appropriately. That is the combination of the random noise sources measured

in the lab (photon noise and dark noise) will be set to be the same combination of random noise sources for the flight mission. The difference is that the flight mission will have lower dark current, and those lower dark noise, thus the photon noise in flight will be a larger contributor to the total noise in flight, but it's the total random noise that will be matched between flight and testbed.

Milestone 3 is also designed to take the following known limitations of HCIT hardware into account:
(1) In HCIT, the communication with the DM and the WFS camera is slow and not optimized for real-time control. The maximum control loop rate allowed by HCIT hardware is >1 Hz, so we will need to artificially slow down both the control and disturbance frequencies by at least a factor of 100. In doing so, we are specifically demonstrating the sensing technique, its closed-loop performance in terms of residual OPD variance, and comparing with the theoretical models in Potier et al. (2021). Developing and demonstrating the real-time computing and control hardware is outside of the scope of this proposal. Otherwise, the experiments are tailored to match a realistic flight scenario to the extent possible.

(2) The wavefront sensor noise floor on DST was measured to be ~30 pm RMS, which is mostly due to detector noise (Ruane et al. 2020). Averaging out these testbed specific noise sources may be extremely time consuming. We will therefore use a relatively large disturbance of 100 pm RMS to ensure we can confidently demonstrate the expected OPD variance rejection factor without being limited by the testbed. As a result, we will also need to artificially scale the noise in the wavefront sensor images such that the S/N of the wavefront measurement is equivalent for a 30 pm RMS disturbance in flight.

The raw contrast contribution of the dynamic errors is proportional to the OPD variance in most cases (there are some exceptions for low order aberrations). Therefore, we expect a proportional reduction in the raw contrast component due to the injected dynamic errors. We will use the measured improvement in the dark hole contrast as compared to our expectation as a verification.

The significance of milestone 3 is to show that the telescope stability requirements of 10 pm RMS are effectively relaxed at temporal frequencies <1 Hz for a future IR/O/UV telescope with AO control capability. Assuming a 100 Hz control loop, the relaxation in OPD variance requirements is given by the transfer function in Fig. 5, left. For instance, if we assume the original telescope stability requirement without AO control is 10 pm RMS, the requirement is relaxed to 30 pm RMS for disturbances <1 Hz and 300 pm RMS at <0.1 Hz.

If all three milestones are achieved in our allotted testbed time, we will explore the limitations of the closed-loop control on HCIT by reducing the injected disturbance amplitude, the effective control loop frequency, and the effective brightness of the guide star. We will also investigate potential improvements, including (1) alternative coronagraph designs to increase throughput, bandwidth, or dark hole size and (2) predictive control laws as demonstrated in Potier et al. (2021).

This method of wavefront sensing is independent of the primary mirror architecture. It will work with both continuous and segmented (even sparse) apertures. Thus, investment in this activity supports a broad range of possible architectures.

3.1 Applicability to Direct Detection Missions

The dual-purpose coronagraphic mask will advance wavefront sensing and control for all direct detection methods using internal coronagraphs. This approach will relax the observatory requirements with a direct impact on mission cost. This method will work with both segmented and continuous primary mirrors.

Any visible-light coronagraph instrument intended to image exoplanets in reflected light has very tight wavefront tolerances. While the coronagraph masks can be optimized to relax low order requirements (Riggs 2021, Ruane 2019), the wavefront stability requirements at mid spatial frequencies are on the order of 10 pm regardless of the coronagraph design. Building a ~6-meter space telescope that provides a wavefront that is stable to 10 pm over the timescale of an observation (i.e., potentially many hours) is extremely challenging, if not impossible, without active compensation. Internal metrology in the telescope can help maintain alignment and prevent rigid body motions. While very useful, these systems only correct motions of specific components and don't necessarily provide the wavefront stability required at the coronagraph.

A recent study led by Axel Potier, a postdoctoral scholar on our team, investigated the performance of a coronagraph instrument with a closed-loop AO system on a LUVOIR-like telescope with realistic vibrations (Potier et al, 2021). Figure 5, reproduced from this work, highlights a key trade-space in the system-level design of a future flagship mission. In order to achieve a raw contrast of 1e-10, either the telescope vibrations need to contribute <10 pm RMS to the wavefront error or there needs to be enough photons available for wavefront sensing on the timescale of the wavefront disturbances. With sufficient photon flux at the wavefront sensor, even the wavefront from a telescope with vibrations on the order of 100 pm RMS can be stabilized enough to provide 1e-10 contrast. However, for vibrations with temporal frequencies >~1 Hz, it is difficult to sense the wavefront changes quickly enough using the out-of-band flux from a natural star. In these scenarios, we invoke the use of a laser guide star (external beacon potentially a separate formation-flying spacecraft) or internal laser source to increase the photon flux at the wavefront sensor. The solution we propose here is compatible with all of the potential solutions in this trade space. Our proposed wavefront sensor can be optimized to a given telescope design or mission by changing the pixel sampling across the beam, the wavelengths of operation, as well as the spatial and temporal bandwidths of the wavefront measurements. It is also compatible with the laser guide star solution mentioned above. (This proposal will use out-of-band stellar photons. Studies for use of a separate, external beacon are beyond the scope of this work.)

The discussion of an off-axis target is an interesting one. Our proposal has always assumed that the science star, and any pseudo-star or beacon, is on axis. If this original intent is not changed, then the masks developed in this SAT would be identical for flight: the Zernike mask used in reflection would be concentric with the coronagraphic mask.

However, in principle, if the pseudo star can be located off-axis, then the Zernike mask can also be moved off center from the coronagraphic mask. Indeed, one could consider both an on-axis and one or more off-axis Zernike phase mask(s). Assuming both beacon and science are on axis, there is no change in the dual-purpose mask design. Regarding target brightness, as mentioned previously, the precision of the sensor is ultimately set by the level of random noise for a given

measurement time (assuming that systematic errors don't introduce a bias.) Assuming we are photon noise limited, then longer integration times (more photons) are needed to achieve a requisite phase noise.

The details of the implementation of the off-axis source are beyond the scope of this work. Yes - we recognize there are engineering challenges in the implementation. Here we simply note a bright pseudo-star that is coincident on the focal plane can shorten measurements times with no change to the focal plane mask itself.

Analysis has been done in the work by Ruane to calculate the time required to achieve picometer level sensitivity for stars of different brightness. This is shown below in Table 1. This table represents the time required to sense the wavefront to picometer precision. A detailed discussion of the wavefront control is beyond the scope of this work.

The benefit of our architecture is that the wavefront sensing and high-contrast imaging are done with an absolute minimum of non-common path: the sensor measures the wavefront where it matters – at the coronagraphic focal plane mask. The mechanical stability of the focal plane mask is thus identical to the tip/tilt sensitivity of the coronagraph because motion of the stellar PSF on the mask is identical to mechanical translation of the mask. Since we measure tip/tilt aberrtion, we actively control this error.

Table 1-2: Estimated integration times using the primary starlight for wavefront sensing in B, V, R and I filters (λ_0 = 438, 545, 641 and 798 nm, respectively) with 64 pixels across the beam in the HabEx coronagraph instrument. The 11 stars are representative of the full range of spectral types. Those labeled with an asterisk * are 'deep dive' targets.

			Integration time (min)			
Star name	Type	Dist (pc)	*B*	*V*	*R*	*I*
Procyon	F5IV-V	3.5	24.4	29.7	32.7	51.2
eta Cas	G0V	5.8	82.6	85.8	88.7	123
tau Ceti*	G8V	3.6	39.8	35.3	33.6	42.1
82 Eri*	G8V	6.0	108	96.6	91.9	123
sig Dra*	K0V	5.8	112	94.6	88.3	117
40 Eri*	K1V	5.0	89.0	72.8	64.3	82.1
GJ 570 A*	K4V	5.9	195	122	82.4	96.0
eps Ind*	K5V	3.6	73.6	48.2	45.9	52.0
61 Cyg A*	K5V	3.5	78.2	45.5	29.9	31.8
61 Cyg B*	K7V	3.5	134	67.4	37.6	21.7
AX Mic	M1/M2V	4.0	222	107	94.2	66.7
Number of stars with lowest τ			10/50	5/50	26/50	9/50

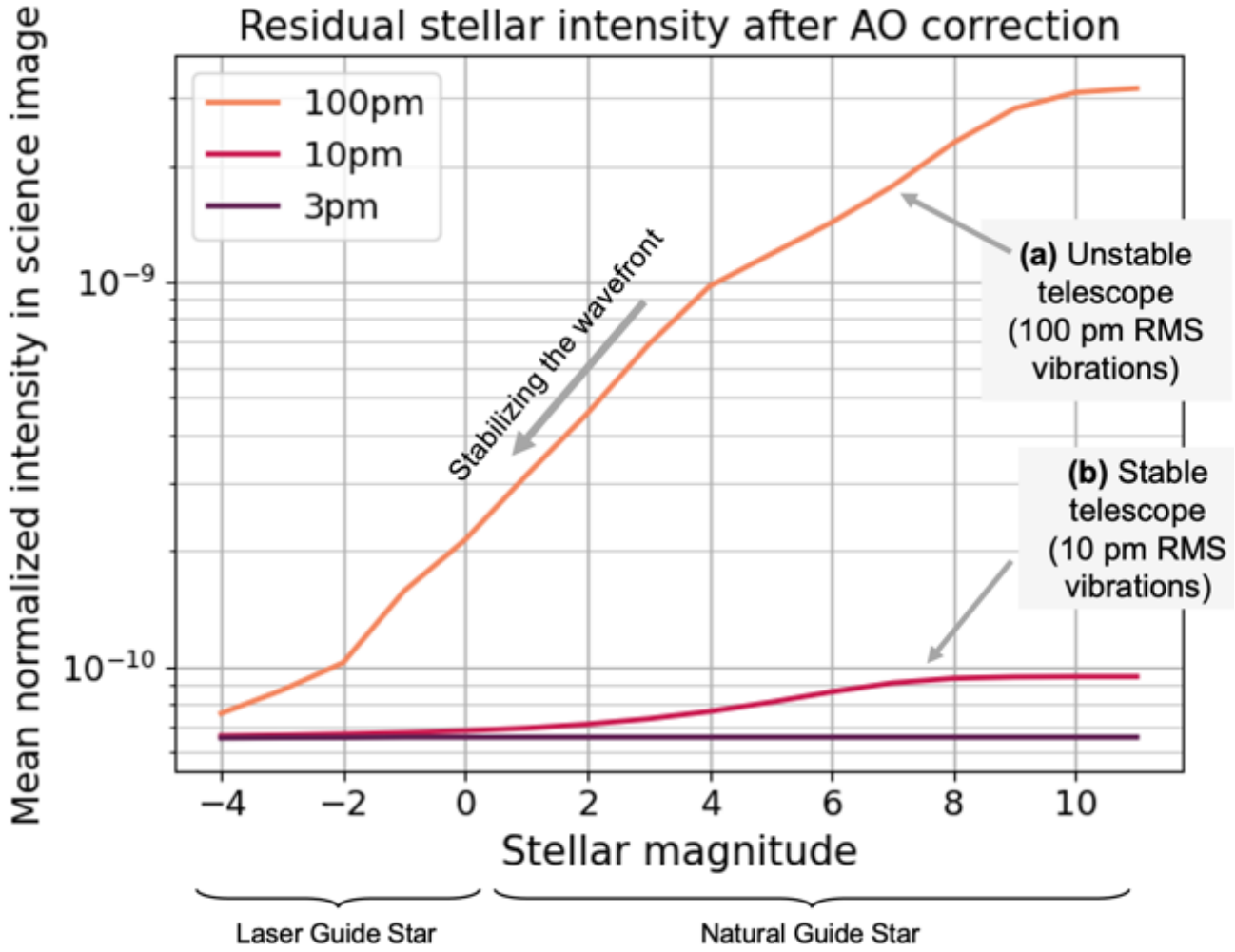

Figure 6. Coronagraph performance versus the brightness of the "star" used for wavefront sensing for the case of (a) an unstable telescope with 100 pm RMS vibrations and (b) a more stable telescope with 10 pm RMS vibrations. In this example, when enough photons are available for wavefront sensing during the time scale of an oscillation in the telescope, the AO system can compensate and restore the coronagraph performance (Potier et al, 2021).

4. Testbed Description

We plan to carry out the proposed work in the High Contrast Imaging Testbed (HCIT) facility at NASA's Jet Propulsion Laboratory (see Fig. 7).

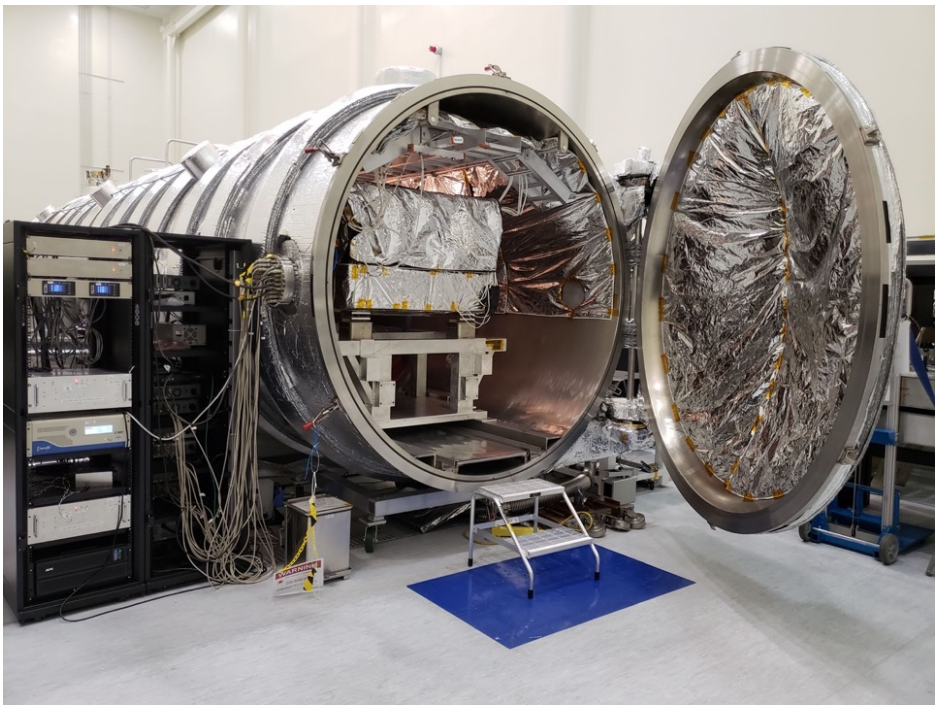

Figure 7. The original Decadal Survey Testbed (DST-1) in the High Contrast Imaging Testbed (HCIT) facility at NASA's Jet Propulsion Laboratory.

4.1 The Decadal Survey Testbeds

As of Spring 2022, there will be two Decadal Survey Testbeds (DST) in a vacuum chamber in the HCIT facility, known as DST-1 and DST-2 [Meeker et al., 2021]. Both have all of the equipment needed for the proposed work except for the Dual-Purpose Masks (DPMs) that we propose to test. The DPMs are designed to be compatible with the focal ratio of the testbeds (F/30) and fit within the mechanical focal plane mask mounts on the DSTs. Either DST testbed would be sufficient to demonstrate the high-contrast and wavefront sensing capabilities of the DPMs (see Fig. 8). For high contrast imaging, the required hardware consists of at least one deformable mirror (DM), a focal plane mask (FPM) mount, Lyot stop (LS), field stop (FS), and science camera. In addition, the wavefront sensing demonstration requires a second camera that receives the light reflected from the focal plane mask with fore-optics that create an image of the plane of the DM on the detector. The DSTs are specifically designed to enable this type of system-level demonstrations for coronagraph instruments.

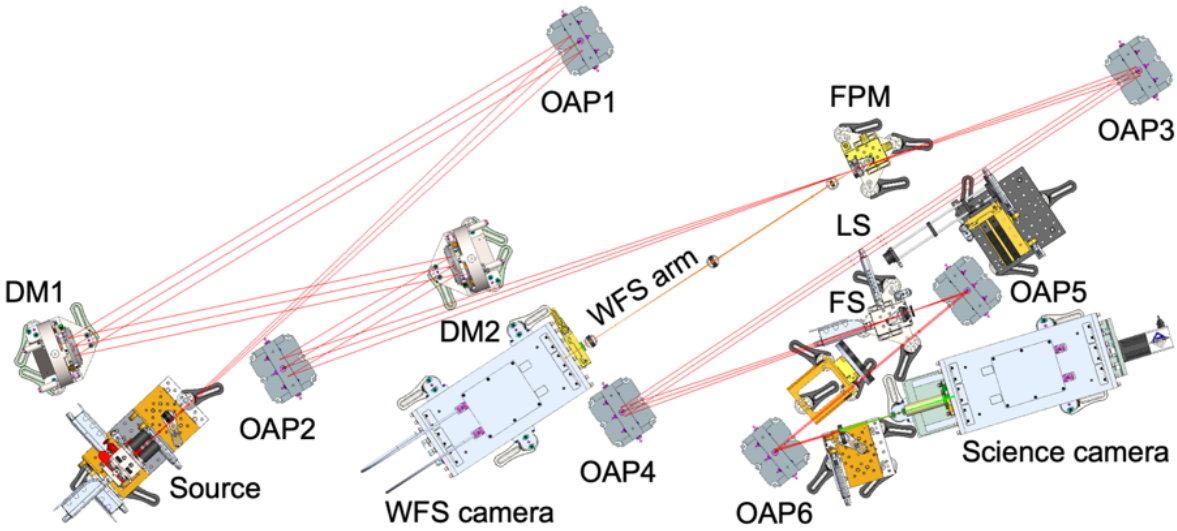

Fig.8. The Decadal Survey Testbed (DST-1) in the HCIT is a coronagraph instrument simulator with two cameras: the science camera and the wavefront sensing (WFS) camera. The high-contrast image of the astrophysical scene appears on the science camera. The WFS camera sees the light reflected from the focal plane mask in the form of a pupil image. The Dual Purpose Masks in the focal plane are designed to provide high-contrast on the science camera while allowing wavefront sensing at high spatial and temporal frequencies on the WFS camera. DM: Deformable mirror. OAP: Off-axis parabola. LS: Lyot stop. FS: Field stop.

4.2 Mask characterization

The Lyot-style mask fabrication includes sourcing glass substrates from optical manufacturers and subcontracting the optical coating deposition as well as photomasking and etching to achieve the desired transmittance and reflectance patterns. The mask is a combination of a substrate with a multilayer dielectric coating for the wavelength separation. On this 'cold mirror' is then deposited a coronagraphic mask (aluminum disk ~ 6 λ/D in diameter) upon which is depositd the Zernike mask (~ 2 λ/D in diameter). There are vendors that specialize in the design and fabrication of the custom multilayer dielectric coating. These vendors have excellent knowledge of the material properties of the materials being deposited, and they are very well versed with the coating metrology as well. That's why we will not do the dielectric coating in house. There are many vendors for this work within short driving distance of JPL. We think the risk of this step is small. However, in order to mitigate against these risks, we will work closely with these coating vendors to make sure they understand our requirements. Vortex-style masks are sourced from specialized manufactures as well. JPL's Microdevices Laboratory has the capability of manufacturing Lyot coronagraph masks, and we will consider using these services depending on cost and schedule.

Our team at JPL has access to optical equipment that will allow us to characterize the manufactured DPMs in detail, including (1) transmission and reflectivity measurements versus wavelength to verify dichroic coatings, (2) polarization-sensitive microscope images to understand the impact of retardance errors due to the coating materials, and (3) surface profiling to measuring the step heights on the coronagraph mask surfaces.

We have some concerns about the impact of the multilayer coating thickness on the coherence (and phase dispersion) of the reflected light. We are maturing our detailed models of the coating, and also devising a metrology system to characterize the coatings. Only after the first dielectric is made, and the devices are tested using our metrology system, will we know if our understanding of the coating physics is complete. This information will then better prepare us for a second iteration of fabrication if we learned something that could be improved with another go.

5. Data Measurement and Analysis

5.1. Definitions

The "normalized intensity" metric used in HCIT requires a measurement of the intensity of speckles appearing within the dark field, relative to the intensity of the incident star. This metric is used as a proxy for "raw contrast," but differs in that normalized intensity doesn't account for field dependent throughput changes due to the coronagraph. The performance will be assessed in terms of statistical confidence of the measured normalized intensity to capture the impact of experimental noise and uncertainties. In the following paragraphs we define the terms involved in this process, spell out the measurement steps, and specify the data products.

5.1.1. "Raw" Image and "Calibrated" Image. Standard techniques for the acquisition of images are used. We define a "raw" image to be the pixel-by-pixel image obtained by reading the charge from each pixel of the CMOS or CCD, amplifying and sending it to an analog-to-digital converter. We define a "calibrated" image to be a raw image that has had background bias subtracted. Saturated images are avoided in the case of CCDs in order to avoid the confusion of CCD blooming and other potential CCD nonlinearities. All raw images are permanently archived and available for later analysis.

5.1.2. We define "scratch" to be a DM setting in which actuators are set to a predetermined surface figure that provides a wavefront that is approximately flat.

5.1.3. We define the "star" to be a small pinhole illuminated with laser or narrowband light relayed via optical fiber from a source outside the HCIT vacuum wall (e.g., a laser or a filtered super-continuum white light source). The "small" pinhole is to be unresolved by the optical system; e.g., on DST, the effective resolution is 18 μm at a wavelength of 550 nm making the pinhole unresolved with a diameter that is 20% of the angular resolution.

5.1.4. We define the "algorithm" to be the computer code that takes as input the measured speckle field image, and produces as output a voltage value to be applied to each actuator of the DM, with the goal of reducing the normalized intensity in a predefined dark zone.

5.1.5. The "normalized intensity" is a dimensionless map representing, for each pixel of the detector, the ratio of its value to the value of the peak of the central PSF that would be measured in the same testbed conditions (light source, exposure time, Lyot stop, etc.) if the coronagraph focal plane mask were removed.

5.1.6. The "mean normalized intensity" is a dimensionless quantity that is the average value of the normalized intensity over the dark zone and spectral range adopted for the experiment.

5.1.7. "Statistical Confidence". The interpretation of measured numerical intensity values shall take into consideration, in an appropriate way, the statistics of measurement, including detector read noise, photon counting noise, and dark noise.

The milestone objective is to demonstrate with high confidence that the true contrast value in the dark field, as estimated from our measurements, is equal to or better than the required threshold contrast value C_0. The estimated true contrast value shall be obtained from the average of the set of four or more contrast values measured in a continuous sequence (over an expected period of approximately one hour).

For example, our milestone with required mean contrast value of $C_0 = 1.0 \times 10^{-9}$ shall be demonstrated with a confidence coefficient of 0.90 or better. Estimation of this statistical confidence level requires an estimation of variances. Given that our speckle fields contain a mix of static and quasi-static speckles (the residual speckle field remaining after the completion of a wavefront sensing and control cycle, together with the effects of alignment drift following the control cycle), as well as other sources of measurement noise including photon detection statistics and detector noise, an analytical development of speckle statistics is impractical. Our approach is to compute the confidence coefficients on the assumption of Gaussian statistics, but also to make the full set of measurement available to enable computation of the confidence levels for other statistics.

At any time in the demonstration, the true contrast is subject to laboratory conditions, including the quality of the optical components, their alignment, any drift in their alignment over time, and the effectiveness of each wavefront sensing and control cycle. With each iteration, our nulling procedure attempts to improve the contrast value, thus compensating for any drift or changes in alignment that may have occurred since the previous iteration, and further variations may be expected due to experimental noise and any limitations in the algorithm. The data set built up from a sequence of such iterations will provide a distribution of contrast values, which will be regarded as Gaussian about a mean contrast for the data set. We therefore consider the mean contrast value as representative of the true contrast value for a data set, and the distribution of contrast determinations among the iterations within the data set as a combination of both random wavefront control errors and random measurement errors.

The mean contrast values and confidence limits are computed in the following manner. The average of one or more images taken at the completion of each iteration is used to compute the contrast value c_i. The mean contrast for a set of images taken in a given sequence is:

$$\hat{c} = \sum_{i=1}^{n} \frac{c_i}{n}$$

where n is the number of images in each set. The standard deviation σ_{each} in the contrast values c_i obtained for individual images within the set, which now includes both the measurement noise and the (assumed random) contrast variations due to changes in the DM settings for each speckle nulling iteration, is:

$$\sigma_{each} = \sqrt{\sum_{i=1}^{n} \frac{(c_i - \hat{c})^2}{n-1}}$$

Our estimate $\hat{c}$ is subject to uncertainty in the contrast measurements $\sigma_{mean} = \sigma_{each} / n$ and the independently-determined overall errors in photometry σ_{phot}. With the approximation that the contrast values have a Gaussian distribution about the mean contrast, the statistical confidence that the mean contrast is less than $C_o = 1 \times 10^{-9}$ is given by:

$$\sigma_{conf} = \frac{1}{\sqrt{2\pi}} \int_{-\infty}^{t} e^{-z^2/2}\, dz$$

where $t = (C_o - \hat{c})/\sigma$ *and* $\sigma = \mathrm{Sqrt}\,[\sigma^2_{mean} + \sigma^2_{phot}]$. The values $\hat{c}$ and σ are the milestone metrics. The 90% confidence value is the value C_0 such that *conf* (C_0) = 0.9 according to the above equations.

5.2. Measurement of the Star Brightness

The brightness of the star is measured with the following steps.

5.2.1. The vortex mask is laterally offset by approximately 10 λ/D or so, so as to transmit maximum stellar flux. Separately, the mask will be slowly stepped off axis and the radial throughput function measured.

5.2.2. To create the photometric reference, a representative sample of short-exposure (e.g., a few milliseconds) images of the star is taken, with all coronagraph elements other than focal-plane vortex mask in place.

5.2.3. The images are averaged to produce a single star image. The "short-exposure peak value" of the star's intensity is estimated. Since the star image is well-sampled in the focal plane (the Airy disk is typically sampled by ~10 pixels within a radius equal to the full width half maximum), the star intensity can be estimated using either the value of the maximum-brightness pixel or an interpolated value representative of the apparent peak.

5.2.4. The "peak count rate" (counts/sec) is measured for exposure times of microseconds to tens of seconds.

5.3. Measurement of the Coronagraph Contrast

Each normalized intensity measurement is obtained as follows:

5.3.1. The vortex mask is centered on the star image.

5.3.2. An image (typical exposure times are ~ tens of seconds) is taken of the coronagraph field (the suppressed star and surrounding speckle field). The dimensions of the target areas, as shown schematically in Figure 9, are defined as follows: A dark (D- shaped) zone representing a useful inner search space, is bounded by a straight line that passes 3 λ / *D* from the star at its closest point, and by a circle of radius 8 λ / *D* centered on the star.

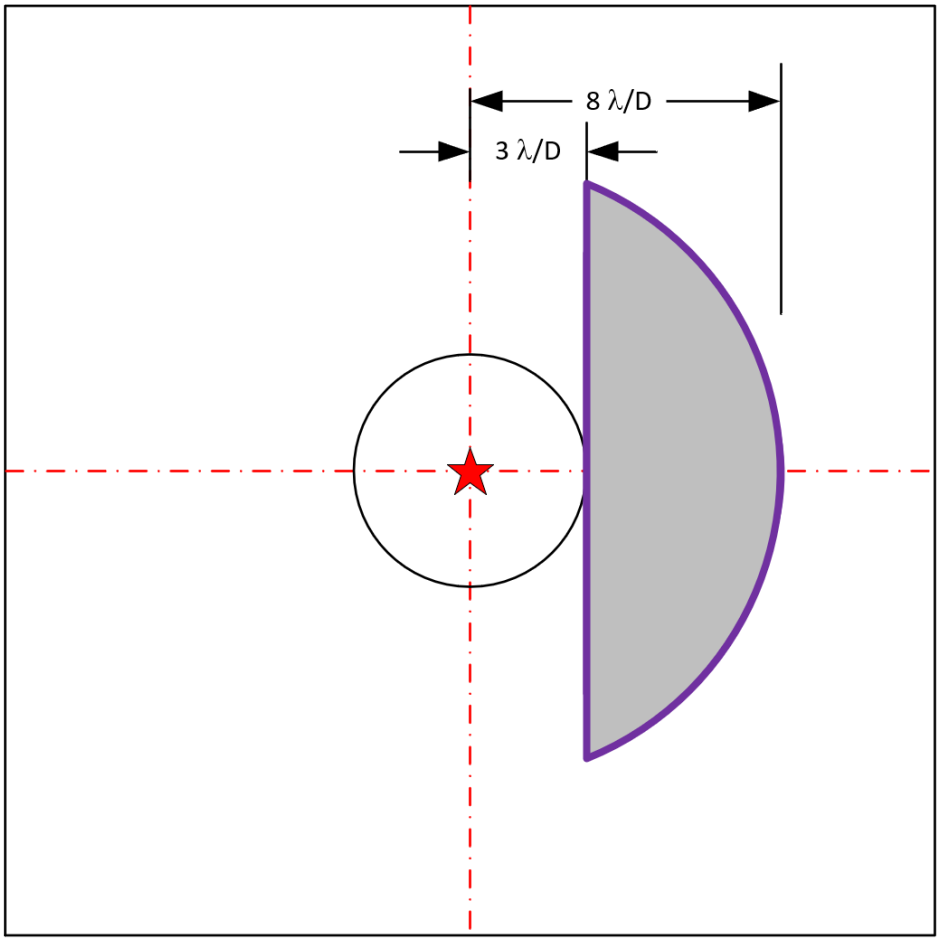

Figure 9. Target high-contrast dark field. As described in the text, inner and outer regions are defined for the one-sided dark field. The location of the suppressed central star is indicated in red. The target dark hole for this initial demonstration would be from 3 to 8 λ/D, as defined in this figure.

5.3.3. The image is normalized to the "peak count rate." Care will be taken to ensure the detector bias is also measured from pixels where incident light in the blocked by the field stop.

5.3.4. The normalized intensity image is averaged over the target dark zones, to produce the estimated raw contrast value. To be explicit, the contrast value is the sum of all contrast values, computed pixel-by-pixel in the dark field area, divided by the total number of pixels in the dark field area, without any weighting being applied. The rms contrast in a given area can also be calculated.

5.4. Milestone Demonstration Procedure

The procedure for the milestone demonstration is as follows:

5.4.1. The DM is set to scratch. An initial coronagraph contrast field image is obtained as described in Sec. 3.3.

5.4.2. Wavefront sensing and control is performed to find settings of the DM actuators that give the required high-contrast in the target dark zone. This iterative procedure may take from one to several hours, starting from scratch, if no prior information is available.

5.4.3. A number of contrast field images are taken. The result at this point is a set of normalized intensity images. It is required that a sufficient number of images are taken to provide statistical confidence that the milestone contrast levels have been achieved.

5.4.4. Laboratory data are archived for future reference, including raw and calibrated images of the reference star and contrast field images.

6. Success Criteria

The following are the required elements of the milestone demonstration. Each element includes a brief rationale.

6.1. Illumination is monochromatic (or a few percent bandwidth) light in single or dual polarization at a wavelength in the range of 400 nm < λ < 900 nm.

6.2. Normalized intensity measurements shall be reported with a confidence of 90% or better. Sufficient data must be taken to justify this statistical confidence.

6.3. Milestones must be satisfied on three separate occasions with a full re-calibration between each demonstration, including new photometric measurement of the pseudo star, detector dark bias, and re-established coronagraph alignment.

7. Schedule

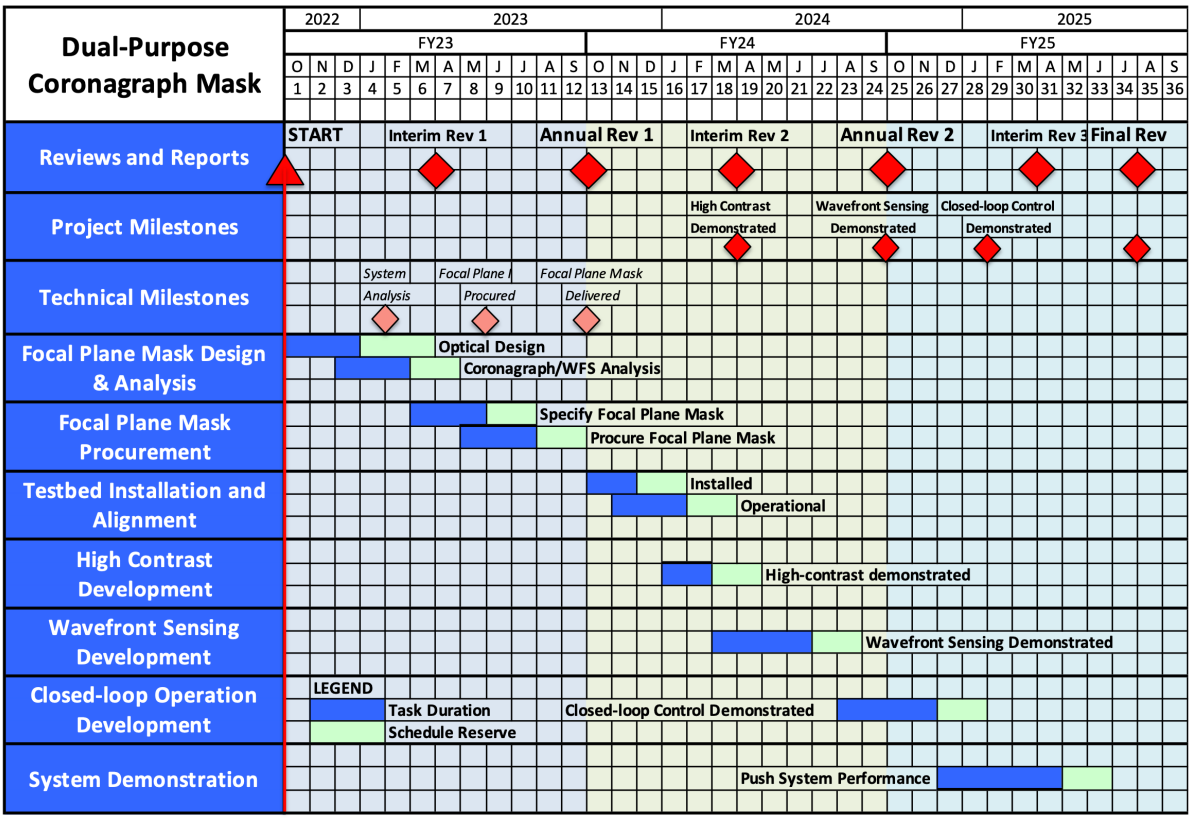

8. References

1. R. H. Dicke, “Phase-contrast detection of telescope seeing errors and their correction,” Astrophys. J. 198, 605–615 (1975).
2. T. D. Groff, A. J. E. Riggs, B. Kern, and N. J. Kasdin, “Methods and limitations of focal plane sensing, estimation, and control in high-contrast imaging,” J. Astron. Telesc. Instrum. Syst. 2(1), pp. 1 – 15, 2015.
3. O. Guyon, “Limits of Adaptive Optics for High-Contrast Imaging” Astrophys. J. 629, 592 (2005)
4. HabEx Study Team, “The habitable exoplanet observatory (HabEx) mis- sion concept study final report,” 2019, https://www.jpl.nasa.gov/habex/ pdf/HabEx-Final-Report-Public-Release.pdf.
5. The LUVOIR Team, “The large UV optical infrared surveyor (LUVOIR) final report,” 2019, https://asd.gsfc.nasa.gov/luvoir/resources/docs/ LUVOIR_FinalReport_2019-08-26.pdf.
6. D. Mawet, E. Serabyn, K. Liewer, Ch. Hanot, S. McEldowney, D. Shemo, and N. O’Brien, "Optical Vectorial Vortex Coronagraphs using Liquid Crystal Polymers: theory, manufacturing and laboratory demonstration," Opt. Express 17, 1902-1918 (2009)
7. Seth R. Meeker, Matthew Noyes, Hong Tang, Garreth Ruane, Camilo Mejia Prada, Eduardo Bendek, Wesley Baxter, Brendan Crill, A. J. Eldorado Riggs, Phillip K. Poon, Nicholas Siegler, "The Twin decadal survey testbeds in the high contrast imaging testbed facility at NASA’s jet propulsion laboratory," Proc. SPIE 11823, Techniques and

Instrumentation for Detection of Exoplanets X, 118230Y (1 September 2021); https://doi.org/10.1117/12.2594668
8. B. Mennesson, S. Gaudi, S. Seager, K. Cahoy, S. Domagal-Goldman, L. Feinberg, O. Guyon, J. Kasdin, C. Marois, D. Mawet, M. Tamura, D. Mouillet, T. Prusti, A. Quirrenbach, T. Robinson, L. Rogers, P. Scowen, R. Somerville, K. Stapelfeldt, D. Stern, M. Still, M. Turnbull, J. Booth, A. Kiessling, G. Kuan, and K. Warfield, "The habitable exoplanet (HabEx) imaging mission: preliminary science drivers and technical requirements," Proc. SPIE 9904, 99040L (2016).
9. National Academies of Sciences, Engineering, and Medicine. 2021. *Pathways to Discovery in Astronomy and Astrophysics for the 2020s*. Washington, DC: The National Academies Press.https://doi.org/10.17226/26141.
10. Axel Potier, Garreth Ruane, Pin Chen, Ankur Chopra, Larry Dewell, Roser Juanola Parramon, Alison Nordt, Laurent Pueyo, David Redding, AJ Eldorado Riggs, Dan Sirbu, "LUVOIR-ECLIPS closed-loop adaptive optics performance and contrast predictions," Proc. SPIE 11823, Techniques and Instrumentation for Detection of Exoplanets X, 118231L (3 September 2021); https://doi.org/10.1117/12.2595116
11. A. J. Eldorado Riggs, Vanessa Bailey, Dwight C. Moody, Erkin Sidick, Kunjithapatham Balasubramanian, Douglas M. Moore, Daniel W. Wilson, Garreth Ruane, Dan Sirbu, Jessica Gersh-Range, John Trauger, Bertrand Mennesson, Nicholas Siegler, Eduardo Bendek, Tyler D. Groff, Neil T. Zimmerman, John Debes, Scott A. Basinger, N. Jeremy Kasdin, "Flight mask designs of the Roman Space Telescope coronagraph instrument," Proc. SPIE 11823, Techniques and Instrumentation for Detection of Exoplanets X, 118231Y (1 September 2021); https://doi.org/10.1117/12.2598599
12. Garreth Ruane, Dimitri Mawet, A.J. Eldorado Riggs, Eugene Serabyn, "Scalar vortex coronagraph mask design and predicted performance," Proc. SPIE 11117, Techniques and Instrumentation for Detection of Exoplanets IX, 111171F (9 September 2019); https://doi.org/10.1117/12.2528625
13. G. Ruane, J. K. Wallace, J. B. Steeves, et al., "Wavefront sensing and control in space-based coronagraph instruments using Zernike's phase-contrast method," JATIS 6(4), 045005 (2020).
14. B.-J. Seo, F. Shi, B. Balasubramanian, E. Cady, B. Gordon, B. Kern, R. Lam, D. Marx, D. Moody, R. Muller, K. Patterson, I. Poberezhskiy, C. Mejia Prada, A. J. E. Riggs, J. Trauger, and D. Wilson, "Hybrid lyot coronagraph for WFIRST: high contrast testbed demonstration in flight-like low flux environment," Proc. SPIE 10698, p. 106982P, 2018.
15. J. Steeves, J. K. Wallace, C. Kettenbeil, and J. Jewell, "Picometer wavefront sensing using the phase-contrast technique", Optica, Vol. 7, Issue 10, pp. 1267-1274 (2020).
16. John Trauger, Dwight Moody, Brian Gordon, John Krist, Dimitri Mawet, "A hybrid Lyot coronagraph for the direct imaging and spectroscopy of exoplanet systems: recent results and prospects," Proc. SPIE 8151, Techniques and Instrumentation for Detection of Exoplanets V, 81510G (15 September 2011); https://doi.org/10.1117/12.895032
17. F. Zernike, "Diffraction theory of the knife-edge test and its improved form the phase contrast method," Mon. Not. R. Astron. Soc. 94, 377–384 (1934).